The Astrophysical Journal, 749:97 (7pp), 2012 April 20 doi:10.1088/0004-637X/749/2/97

CLASH: NEW MULTIPLE IMAGES CONSTRAINING THE INNER MASS PROFILE OF MACS J1206.2−0847

A. Zitrin[1,2], P. Rosati[3], M. Nonino[4], C. Grillo[5], M. Postman[6], D. Coe[6], S. Seitz[7], T. Eichner[7], T. Broadhurst[8,9], S. Jouvel[10], I. Balestra[11], A. Mercurio[12], M. Scodeggio[13], N. Benítez[14], L. Bradley[6], H. Ford[15], O. Host[10], Y. Jimenez-Teja[14], A. Koekemoer[6], W. Zheng[15], M. Bartelmann[2], R. Bouwens[16], O. Czoske[17], M. Donahue[18], O. Graur[1], G. Graves[19], L. Infante[20], S. Jha[21], D. Kelson[22], O. Lahav[10], R. Lazkoz[8], D. Lemze[15], M. Lombardi[23], D. Maoz[1], C. McCully[21], E. Medezinski[15], P. Melchior[24], M. Meneghetti[25], J. Merten[2], A. Molino[14], L. A. Moustakas[26], S. Ogaz[6], B. Patel[21], E. Regoes[27], A. Riess[6,15], S. Rodney[15], K. Umetsu[28], and A. Van der Wel[29]

[1] The School of Physics and Astronomy, Tel Aviv University, Tel Aviv, Israel; adiz@wise.tau.ac.il
[2] Institut für Theoretische Astrophysik, ZAH, Albert-Ueberle-Straße 2, 69120 Heidelberg, Germany
[3] ESO-European Southern Observatory, D-85748 Garching bei München, Germany
[4] INAF-Osservatorio Astronomico di Trieste, via G.B. Tiepolo 11, 40131 Trieste, Italy
[5] Excellence Cluster Universe, Technische Universität München, Boltzmannstr. 2, D-85748, Garching bei München, Germany
[6] Space Telescope Science Institute, 3700 San Martin Drive, Baltimore, MD 21208, USA
[7] Universitäts-Sternwarte München, Scheinerstr. 1, D-81679 München, Germany
[8] Department of Theoretical Physics, University of Basque Country, P.O. Box 644, 48080 Bilbao, Spain
[9] IKERBASQUE, Basque Foundation for Science, Spain
[10] Department of Physics & Astronomy, University College London, Gower Street, London WC1E 6 BT, UK
[11] Max-Planck-Institut für Extraterrestrische Physik, Postfach 1312, 85741 Garching, Germany
[12] INAF-Osservatorio Astronomico di Capodimonte, via Moiariello 16, I-80131 Napoli, Italy
[13] INAF-IASF Milano, Via Bassini 15, I-20133, Milano, Italy
[14] Instituto de Astrofísica de Andalucía (CSIC), C/Camino Bajo de Huétor 24, Granada 18008, Spain
[15] Department of Physics and Astronomy, The Johns Hopkins University, 3400 North Charles Street, Baltimore, MD 21218, USA
[16] Leiden Observatory, Leiden University, P.O. Box 9513, 2300 RA Leiden, The Netherlands
[17] Institut für Astronomie der Universität Wien, Türkenschanzstraße 17, 1180 Wien, Austria
[18] Department of Physics and Astronomy, Michigan State University, East Lansing, MI 48824, USA
[19] Department of Astronomy, University of California, Berkeley, CA 94720, USA
[20] Departamento de Astronoía y Astrofísica, Pontificia Universidad Católica de Chile, V. Mackenna 4860, Santiago 22, Chile
[21] Deptartment of Physics and Astronomy, Rutgers, The State University of New Jersey, Piscataway, NJ 08854-8019, USA
[22] Observatories of the Carnegie Institution of Washington, Pasadena, CA 91101, USA
[23] Dipartimento di Fisica, Universitá degli Studi di Milano, via Celoria 16, I-20133 Milan, Italy
[24] Center for Cosmology and Astro-Particle Physics, & Department of Physics; The Ohio State University, 191 W. Woodruff Ave., Columbus, Ohio 43210, USA
[25] INAF, Osservatorio Astronomico di Bologna, & INFN, Sezione di Bologna; Via Ranzani 1, I-40127 Bologna, Italy
[26] Jet Propulsion Laboratory, California Institute of Technology, MS 169-327, Pasadena, CA 91109, USA
[27] European Laboratory for Particle Physics (CERN), CH-1211, Geneva 23, Switzerland
[28] Institute of Astronomy and Astrophysics, Academia Sinica, P.O. Box 23-141, Taipei 10617, Taiwan
[29] Max-Planck Institute for Astronomy, Königstuhl 17, D-69117, Heidelberg, Germany
Received 2011 July 13; accepted 2012 February 10; published 2012 March 27

ABSTRACT

We present a strong-lensing analysis of the galaxy cluster MACS J1206.2−0847 ($z = 0.44$) using UV, Optical, and IR, *HST*/ACS/WFC3 data taken as part of the CLASH multi-cycle treasury program, with VLT/VIMOS spectroscopy for some of the multiply lensed arcs. The CLASH observations, combined with our mass model, allow us to identify 47 new multiply lensed images of 12 distant sources. These images, along with the previously known arc, span the redshift range $1 \lesssim z \lesssim 5.5$, and thus enable us to derive a detailed mass distribution and to accurately constrain, for the first time, the inner mass profile of this cluster. We find an inner profile slope of $d\log\Sigma/d\log\theta \simeq -0.55 \pm 0.1$ (in the range $[1'', 53'']$, or 5 kpc $\lesssim r \lesssim$ 300 kpc), as commonly found for relaxed and well-concentrated clusters. Using the many systems uncovered here we derive credible critical curves and Einstein radii for different source redshifts. For a source at $z_s \simeq 2.5$, the critical curve encloses a large area with an effective Einstein radius of $\theta_E = 28'' \pm 3''$, and a projected mass of $(1.34 \pm 0.15) \times 10^{14}\ M_\odot$. From the current understanding of structure formation in concordance cosmology, these values are relatively high for clusters at $z \sim 0.5$, so that detailed studies of the inner mass distribution of clusters such as MACS J1206.2−0847 can provide stringent tests of the ΛCDM paradigm.

Key words: dark matter – galaxies: clusters: general – galaxies: clusters: individual (MACS J1206.2−0847) – galaxies: high-redshift – gravitational lensing: strong

Online-only material: color figures, machine-readable table

1. INTRODUCTION

Massive galaxy clusters, due to their high inner mass density, are known to form prominent gravitational lenses. The expected distribution of lens sizes, and the abundance of giant lenses in particular, have been now established by *N*-body simulations (e.g., Hennawi et al. 2007), semi-analytic calculations (e.g., Oguri & Blandford 2009), and recently, also examined observationally by a statistical analysis and lens modeling of 10,000 SDSS clusters (see Zitrin et al. 2011b).

Due to the hierarchical growth of structure in the universe, collapsed, virialized clusters should be found mostly at lower redshifts. These clusters are excellent lenses as there is more mass concentrated in the cluster center, boosting the critical

lensing area. According to this assumption, along with the dependency on the cosmological distances involved, lensing should be therefore optimized in clusters at redshifts of $z_l \sim 0.2$. However, recent work has uncovered more large higher-redshift ($z_l \sim 0.5$) lenses than expected by ΛCDM and related simulations, even after accounting for lensing bias (e.g., Zitrin et al. 2011a, 2011b; Meneghetti et al. 2011).

The existence of high-redshift massive clusters at $z_l \gtrsim 1$ (Rosati et al. 2009; Fassbender et al. 2011; Gobat et al. 2011; Planck Collaboration et al. 2011; Santos et al. 2011; Williamson et al. 2011), as well as the existence of evolved galaxies at high redshift, and other reported discrepancies such as the arc abundance and high concentrations are also claimed to be unlikely given the predicted abundance of extreme perturbations of cluster-sized masses in the standard ΛCDM scenario (e.g., Daddi et al. 2007, 2009; Broadhurst & Barkana 2008; Broadhurst et al. 2008; Jee et al. 2009, 2011; Richard et al. 2011; Zitrin et al. 2010, 2011a, 2011b, 2011d). These claimed discrepancies possibly point toward a more extended early history of growth, or a non-Gaussian distribution of massive perturbations.

The galaxy cluster MACS J1206.2−0847 ($z = 0.4385$; MACS1206 hereafter) is an X-ray selected system at intermediate redshift found by the Massive Cluster Survey (MACS; Ebeling et al. 2001, 2007, 2010), and therefore constitutes an interesting lensing target. A first mass model for this cluster was presented by Ebeling et al. (2009), based on one-band *Hubble Space Telescope* (*HST*)/Advanced Camera for Surveys (ACS) imaging (F606W), combined with additional optical and NIR ground-based imaging. Ebeling et al. (2009) have identified one multiple system, consisting of a giant arc and its counter image at $z_s = 1.036$, and presented a mass distribution for this cluster, though without constraining the profile due to the lack of sufficient high-resolution color-imaging, and correspondingly, other multiple systems. The 16 *HST* bands chosen for the the Cluster Lensing And Supernova survey with Hubble (CLASH) project (Postman et al. 2012), ranging from the UV through the optical and to the IR, along with spectra from the Very Large Telescope (VLT)/VIMOS for some of the brighter arcs, enable us to obtain accurate redshifts for the multiply lensed sources presented in this work. We use these data available to date, along with our well-tested approach to SL modeling (e.g., Broadhurst et al. 2005; Zitrin et al. 2009a, 2009b, 2010, 2011a, 2011c, 2011d), to find a significant number of multiple images across the central field of MACS1206 so that its mass distribution and inner profile can be constrained for the first time, and with high precision.

The paper is organized as follows: In Section 2 we describe the observations, and in Section 3 we detail the SL analysis. In Section 4 we report and discuss the results. Throughout we adopt a concordance ΛCDM cosmology with ($\Omega_{m0} = 0.3, \Omega_{\Lambda 0} = 0.7$, $h = 0.7$). With these parameters 1 arcsec corresponds to a physical scale of 5.67 kpc for this cluster (at $z = 0.4385$; Ebeling et al. 2009). The reference center of our analysis is fixed on the brightest cluster galaxy (BCG): R.A. = 12:06:12.15, decl. = −08:48:03.4 (J2000.0).

2. OBSERVATIONS AND REDSHIFTS

As part of the CLASH program, MACS1206 was observed with *HST* from 2011 March to 2011 July. This is 1 of 25 clusters to be observed to a depth of 20 *HST* orbits in 16 filters with the Wide Field Camera 3 (WFC3) UVIS and IR cameras, and the ACS WFC. The images are processed for debias, flats, superflats, and darks, using standard techniques, and are then co-aligned and combined using drizzle algorithms to a scale of $0\farcs065$ pixel^{-1} (e.g., see Koekemoer et al. 2002, 2011). The full UVIS/ACS/WFC3-IR data set is then importantly used for multiple-image verification and measurement of their photometric redshifts using both the BPZ program (Benítez 2000; Benítez et al. 2004; Coe et al. 2006) and LePhare (Arnouts et al. 1999; Ilbert et al. 2006), where in practice 15 bands were used for the photometry, as observations for this cluster were still in progress during the preparation of this paper (nearly all 20 orbits had been completed, for most filters. The F336W band was not used). Further details are presented in Postman et al. (2012).

We obtain spectra for a number of multiple systems uncovered here, taken as part of the VLT/VIMOS Large Programme 186.A-0798, which will perform panoramic spectroscopy of 14 southern CLASH clusters, targeting hundreds of cluster members per cluster and SL features in their cores. Details on this program will be presented elsewhere, when observations for one cluster are completed. For each cluster, four VIMOS pointings are used, keeping one of the four quadrants constantly locked on the cluster core, thus allowing long exposures on the arcs, where exposure times for each pointing are about 45–60 minutes. By filling the inter-quadrant gaps, the final VIMOS layout covers $20'$–$25'$ across. Either the low-resolution LR-Blue grism or the intermediate-resolution orange MR grism is used, depending on the photometric redshifts of the targets.

The spectra presented here are the results of the very first observations for this program, consisting of four pointings with the LR-Blue grism, obtained in 2011 March–April, which yielded approximately 1000 redshifts. This configuration provides a spectral resolution of ∼28 Å with $1''$ slits and a useful wavelength coverage of 3700–6800 Å. Preliminary *HST*/CLASH data from the first two visits of MACS1206 were used to select images 1.[1, 2, 3], 2.[1, 2, 3], 3.[1, 2, 3], and 4.1 as spectroscopic targets (see Figure 1). The slits ran along the NS direction. For some exposures, the seeing was very good so that separate spectra of the pairs 2.1/3.1 and 2.2/3.2 (separation of $\sim 1''$) were taken (and are shown in Figure 2, Table 1), though in other cases the pairs were blended in the slit. The spectrum of 1.2, which contains the blend of the giant arc and a compact cluster galaxy, is not shown. A spectrum of this arc, covering redder wavelengths including the [O II] line, was however published in Ebeling et al. (2009). Our spectroscopy also confirms that the four compact galaxies right on the east and west side to the giant arc are early-type cluster members.

3. STRONG-LENSING MODELING AND ANALYSIS

The approach to lens modeling we use here (e.g., Broadhurst et al. 2005; Zitrin et al. 2009b) begins with the assumption that mass approximately traces light, so that the photometry of the red-sequence cluster member galaxies is used as the starting point for our model. In particular, we use the F814W and F475W bands to filter in the brighter member galaxies ($m_{814} < 23$ AB mag), and the F814W flux to derive the relative weight of each member. Using the extensive multi-band imaging and corresponding photometric redshifts, these galaxies can be then verified as members lying at the cluster redshift.

We approximate the large-scale distribution of cluster mass by assigning a power-law mass profile to each galaxy, the sum of which is then smoothed, using a two-dimensional (2D) spline interpolation. The polynomial degree of smoothing (S) and the index of the power law (q) are the most important free parameters determining the mass profile: steeper power laws

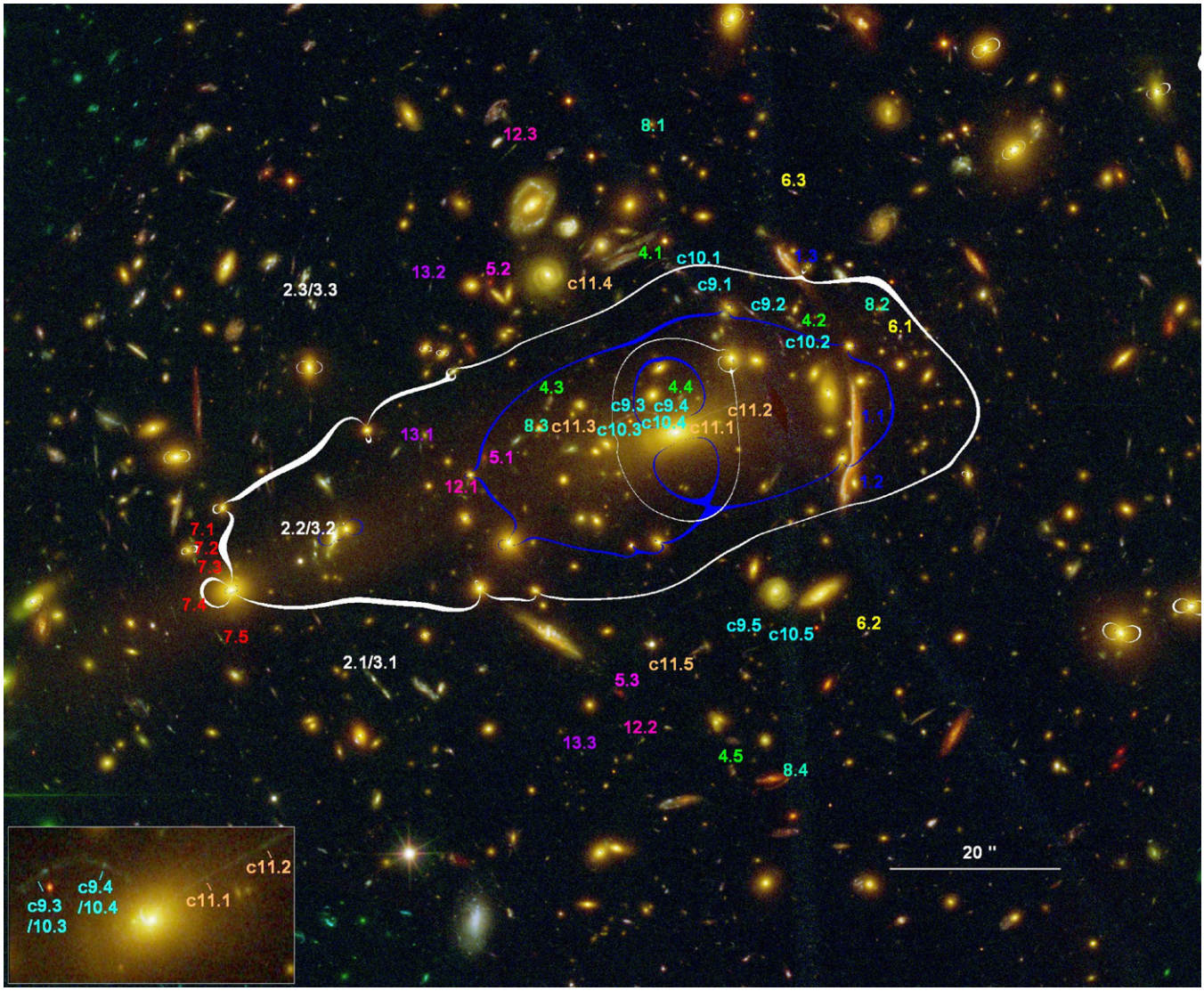

Figure 1. Galaxy cluster MACS1206 ($z = 0.4385$) imaged with *HST*/ACS/WFC3. North is up and east is left. We number the multiply lensed images used and uncovered in this work. The numbers indicate the 50 lensed images, 47 of which are uncovered here and correspond to (at least) 12 newly identified sources and candidates, and the different colors are used to distinguish between them. Note that candidate systems are marked in "c." Details on the each system are given in Table 1. The overlaid white critical curve corresponds to system 4 at $z_s = 2.54$, enclosing a critical area with an effective Einstein radius of $\simeq$160 kpc at the redshift of this cluster (28″). The blue critical curve corresponds to the lower redshift of system 1, the giant arc system at $z_s = 1.033$. The composition of this color image is red = F105W+F110W+F125W+F140W+F160W, green = F606W+F625W+F775W+F814W+F850LP, and blue = F435W+F475W. The bottom left inset shows an enlargement of the central core.

(A color version of this figure is available in the online journal.)

and higher 2D polynomial degrees generally entail a steeper profile (see Zitrin et al. 2009b). A worthwhile improvement in fitting the location of the lensed images is generally found by expanding to first order the gravitational potential of this smooth component, equivalent to a coherent shear describing the overall matter ellipticity. The direction of the shear and its amplitude are free parameters, allowing for some flexibility in the relation between the distribution of dark matter (DM) and the distribution of galaxies, which cannot be expected to trace each other in detail. The total deflection field $\vec{\alpha}_T(\vec{\theta})$, consists of the galaxy component, $\vec{\alpha}_{\rm gal}(\vec{\theta})$, scaled by a factor $K_{\rm gal}$, the cluster DM component $\vec{\alpha}_{\rm DM}(\vec{\theta})$, scaled by $(1 - K_{\rm gal})$, and the external shear component $\vec{\alpha}_{\rm ex}(\vec{\theta})$ is given by

$$\vec{\alpha}_T(\vec{\theta}) = K_{\rm gal}\vec{\alpha}_{\rm gal}(\vec{\theta}) + (1 - K_{\rm gal})\vec{\alpha}_{\rm DM}(\vec{\theta}) + \vec{\alpha}_{\rm ex}(\vec{\theta}), \quad (1)$$

where the overall scaling of this deflection field brings the number of free parameters in our modeling to six.

The best fit is assessed by the minimum χ^2 uncertainty in the image plane:

$$\chi^2 = \sum_i \left(\left(x_i' - x_i\right)^2 + \left(y_i' - y_i\right)^2 \right) / \sigma^2, \quad (2)$$

where x_i' and y_i' are the locations given by the model, x_i and y_i are the real image locations, σ is the one-dimensional (1D) error in the true location measurement (for each of the directions x and y), and the sum is over all N images.

The resulting errors are determined accordingly, by adopting a (2D) positional error of 2″, so that the (1D) term in Equation (2) is $\sigma = 1\farcs4$. We found this to be a typical value, based on previous findings for the effect of substructure in the lens plane and large-scale structure (LSS) along the line of sight (Jullo

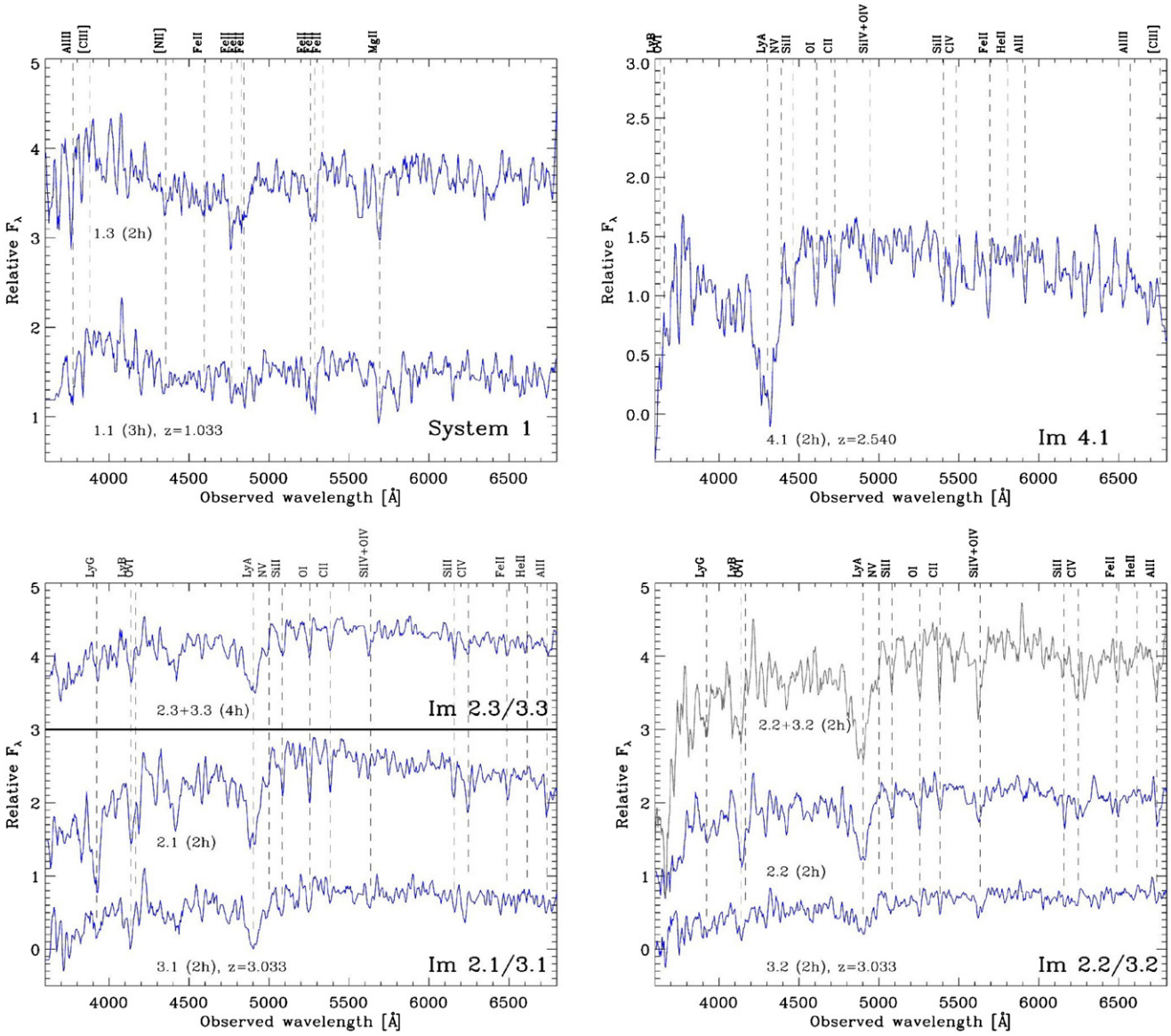

Figure 2. VLT/VIMOS spectra obtained for systems 1–4, at $z_{sys1} = 1.033$, $z_{sys2,3} = 3.033$, and $z_{sys4} = 2.540$. The exposure time for each spectrum is shown in parentheses. For the $z = 3.03$ systems, the pairs are blended into the slits in some cases (2.2+3.2, 2.3+3.3) due to less ideal seeing conditions, though in some exposures the seeing was sufficient to resolve each individually.

(A color version of this figure is available in the online journal.)

et al. 2010; D'Aloisio & Natarajan 2011; Host 2012), and by propagating a typical $\Delta z \sim 0.1$ photo-z uncertainty (for $z_s \sim 2$) into the image-plane reproduction error. Note also that this image-plane minimization does not suffer from the bias involved with source-plane minimization, where solutions are biased by minimal scatter toward shallow mass profiles with correspondingly higher magnifications.

It should be stressed that the multiple images found here are accurately reproduced by our model (e.g., Figure 3) and are not simple identifications by eye. Due to the small number of parameters in our model, it is initially well constrained, enabling a reliable identification of other multiple images in the field. The mass model predictions are identified in the data and verified further by comparing the spectral energy distributions and photometric redshifts of the candidate multiple images. The model is successively refined as additional sets of multiple images are incorporated to improve the fit, and, importantly, using also their redshift information to better constrain the mass slope through the cosmological relation of the D_{ls}/D_s growth.

4. RESULTS AND CONCLUSIONS

Using CLASH imaging, we have identified 47 new multiple images in MACS1206 of 12 new distant sources, so that 50 multiple images are now known in this cluster's field. The multiple images are shown in Figure 1 and listed in Table 1. System 1 consists of a remarkable giant arc and an additional counter image, and was uncovered by Ebeling et al. (2009) who measured the redshift of images 1.1 and 1.2 spectroscopically at $z = 1.036$; our spectroscopy yields $z = 1.033$ for this system. We interpret this long arc (images 1.1/1.2) as a double-lensed image, though Ebeling et al. (2009) identified it to consist of several (partially) lensed images. Either interpretation has only a very local (negligible) effect on the mass model. All other systems listed in Table 1 are found in our work and demonstrate

Table 1
Multiple-image Systems and Candidates

ARC ID	R.A. (J2000.0)	Decl. (J2000.0)	BPZ z_{phot} (best) (95% CL)	LePhare z_{phot} (best) (90% CL)	spec-z	z_{model}	ΔPosition (arcsec)	Comment
1.1	12:06:10.75	−08:48:01.01	– [–]	– [–]	1.033	(1.033)	3.4	
1.2	12:06:10.82	−08:48:08.95	1.04 [0.96–1.12]	1.06 [1.04–1.09]	(1.036)	”	0.1	Ebeling et al. (2009)
1.3	12:06:11.29	−08:47:43.44	1.01 [0.93–1.09]	1.05 [1.03–1.06]	1.033	”	3.3	
2.1	12:06:14.53	−08:48:32.37	– [–]	– [–]	3.03	(3.03)	0.2	
2.2	12:06:15.00	−08:48:17.67	3.40 [3.23–3.57]	3.19 [3.12–3.36]	3.03	”	0.5	
2.3	12:06:15.03	−08:47:48.07	3.68 [3.50–3.86]	3.64 [3.59–3.70]	3.03	”	2.1	
3.1	12:06:14.43	−08:48:34.20	3.73 [3.55–3.92]	3.65 [3.60–3.73]	3.03	(3.03)	0.2	
3.2	12:06:15.00	−08:48:16.50	– [–]	– [–]	3.03	”	0.5	
3.3	12:06:15.01	−08:47:48.65	3.52 [3.34–3.70]	3.62 [3.53–3.67]	3.03	”	2.1	

Notes. Multiple-image systems and candidates used and uncovered by our model. Columns are: arc ID; R.A. and Decl. in J2000.0; best photo-z using BPZ and LePhare, respectively; spectroscopic redshift, spec-z (we obtain VLT/VIMOS spectroscopy for systems 1–4, images marked in parenthesis were not spectroscopically measured here); z_{model}, estimated redshift for the arcs which lack spectroscopy as predicted by the mass model; ΔPosition, difference between the images reproduced by the model and the observed images; comments. Note that unusually large errors in the photo-z imply a bimodal distribution, as specified in the comments. We also denote in the comments column where the most probable image was chosen but other candidates are seen nearby. Systems 9–11 are designated as candidate systems. For more details, see Section 4.

(This table is available in its entirety in a machine-readable form in the online journal. A portion is shown here for guidance regarding its form and content.)

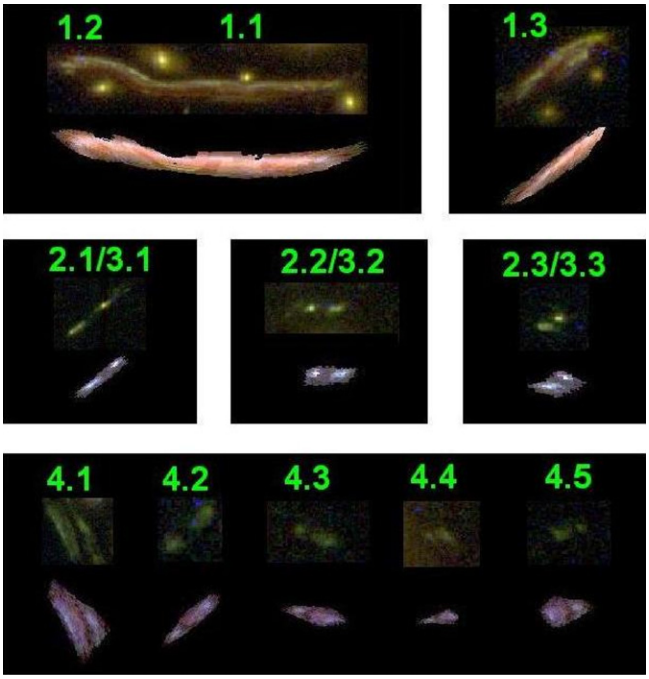

Figure 3. Reproduction of systems 1–4 by our model, compared with the real images. For each system we delens one image to the source plane and relens it back to the image plane to obtain the other images of that system. More explicitly, we delens–relens, respectively, images 1.1, 2.2/3.2, and 4.1, each in the lensing-distance ratio expected from its redshift (1.033, 3.03, 2.54, respectively), to obtain the results shown here. The upper images in each row are the real images while the lower images are those reproduced by our model. As can be seen, our model reproduces the images of these systems with great accuracy. In these stamp images, north is right and east is up, and some of the images are slightly zoomed-in for clarity. Note also, due to their similar position and symmetry, systems 2 and 3 were considered a single system in the minimization of the mass model.

(A color version of this figure is available in the online journal.)

once more the success of our modeling technique in physically finding multiple images, and correspondingly, generating a reliable mass model.

We obtained VLT/VIMOS spectra for systems 1–4, at redshifts 1.033, 3.03, 3.03, and 2.54, respectively, which help us pin down the mass model, and especially the profile, with greater accuracy. As can be seen in Figure 1, systems 2 and 3 consist of two nearby sources following similar symmetry, east of the BCG. System 4 consists of five bluish–reddish images with distinguishable internal detail, which form around the central core and thus supply important constraints to accurately map the inner mass distribution. Systems 5, 6, 12, and 13 follow the same symmetry as systems 2 and 3 all across the critical curves, and system 7 comprises five images next to bright cluster members and helps constrain the eastern edge of the critical curves. System 8 comprises four images of a high-z source at $z \sim 5.5$, supplying an important constraint on the mass profile.

Systems 9–11 are designated as candidate systems, since only some of the ($<1\sigma$) models can reproduce them, or simply since their photo-z disagrees with the model prediction. Also, systems 9 and 10 show similar symmetry to that of system 4, strengthening their identification on one hand, but only two radial images are seen in the data. Due to the BCG light it is hard to determine unambiguously if, or to which, of these two systems they belong. Note also that if images 11.1 and 11.2 are not multiple images, but, say, a jet coming out of the BCG (see inset in Figure 1), then images 11.3–11.5 may constitute an individual system. All other systems we consider secure identifications, in the context of the photometric redshifts, internal details, and the reproduction by our model. In Figure 3, we show examples for reproductions of some of the multiple systems by our model.

The high number of new multiple images found in this work, along with the previously known arc (Ebeling et al. 2009), span the redshift range $1 \lesssim z \lesssim 5.5$ and thus allow us to derive a robust mass distribution and constrain the profile of this cluster, for the first time. We made use of the location and redshift of all secure multiple images (i.e., excluding candidate systems 9–11) to fully constrain the mass model and profile. The χ^2 for the best model is 51.5. To assess the goodness of fit we calculate the *reduced* χ^2, simply by dividing the χ^2 by the number of degrees of freedom (DOF) which is given by

$$\mathrm{DOF} = N_c - N_p, \tag{3}$$

where N_p is the number of free parameters in our modeling, and N_c is the number of constraints given by

$$N_c = \nu(N_{\mathrm{im}} - N_s), \tag{4}$$

where the number of dimensions is $\nu = 2$ since each image (and source) is characterized by two measures (x and y; see Equation (2)), $N_{\rm im}$ is the total number of images used for the fit, and N_s is the number of systems (or sources). This stems from the fact that each system contributes $\nu(N-1)$ constraints, where N is the number of images in that system, and one needs to sum over all systems (see also Kneib et al. 1993 for a general formalism). With 32 secure multiply lensed images used for constraining the fit, belonging to nine sources (systems 2 and 3 were treated as one system), Equation (4) yields $N_c = 46$ constraints. Since we have $N_p = 6$ model parameters, there are thus 40 DOF (Equation (3)), yielding a *reduced* χ^2 of 1.29. We note that there is a probability of 10.5% to get a χ^2 of 51.5 or higher, for 40 DOF.

Estimating the accuracy of our mass distribution quantitatively, for all secure images we obtain an average image-plane reproduction uncertainty of 1.″3 per image, with an image-plane rms of 1.″8, typical of parametric mass models for clusters with many multiple images (Broadhurst et al. 2005; Halkola et al. 2006; Limousin et al. 2007; Zitrin et al. 2009b). Note that these values are obtained by delensing each of the images of a certain system to the source plane, and then relensing back to the image plane the average source position of that system. This information is important to include in order to compare between different SL methods. Although it constitutes a standard estimator of SL models, the rms is quite a sensitive measure. It is naturally coupled to the numerical method in which it is calculated, and is highly susceptible to single outliers, so that due to the relatively low number of multiple images in lensing clusters, it is dependent in practice on the specific multiple-image systems incorporated. The rms value we obtain is realistic given the $\sim 1''$ noise level expected from LSS along the line of sight (e.g., Jullo et al. 2010; D'Aloisio & Natarajan 2011; Host 2012), the many multiple images used, and the small number of free parameters in our modeling.

For a source at $z_s = 2.54$, the critical curves enclose a relatively large area, with an effective Einstein radius of $r_E = 28 \pm 3''$, or $\simeq$158 kpc at the redshift of the cluster. A projected mass of $(1.34 \pm 0.15) \times 10^{14}\, M_\odot$ is enclosed by this critical curve for this source redshift (see Figure 1). For the lower source redshift of system 1, $z_s = 1.033$, the Einstein radius is $\simeq 17''$, enclosing a projected mass of $(0.8 \pm 0.1) \times 10^{14}\, M_\odot$. For comparison, our model encloses within 21″ a projected mass of $M(< 21'') \simeq (1 \pm 0.1) \times 10^{14}\, M_\odot$, while Ebeling et al. (2009) similarly found, although based on only one system, a projected mass of $M(< 21'') = (1.12 \pm 0.05) \times 10^{14}\, M_\odot$, consistent with our result. In addition, as a consistency check for the very inner profile around the BCG, we compared our result to the F160W light. By estimating the stellar mass profile from the F160W surface brightness photometry, assuming a Kroupa IMF, the stellar mass is approximately 10% of the total mass within 30 kpc, which is approximately half the BCG effective radius. We defer to forthcoming papers the exact assessment of the DM mass distribution steepness in the very inner region (say, below ~5 kpc) after taking into account the stellar and gas baryonic contributions.

The corresponding critical curves for different redshifts are plotted on the cluster image in Figure 1, along with the multiply lensed systems. The resulting total mass profile is shown in Figure 4, for which we measure a slope of $d\log\Sigma/d\log r \simeq -0.55 \pm 0.1$ (in the range [1″, 53″], or 5 kpc $\lesssim r \lesssim$ 300 kpc; about twice the Einstein radius), similar to other usually relaxed and well-concentrated lensing clusters (Broadhurst et al. 2005;

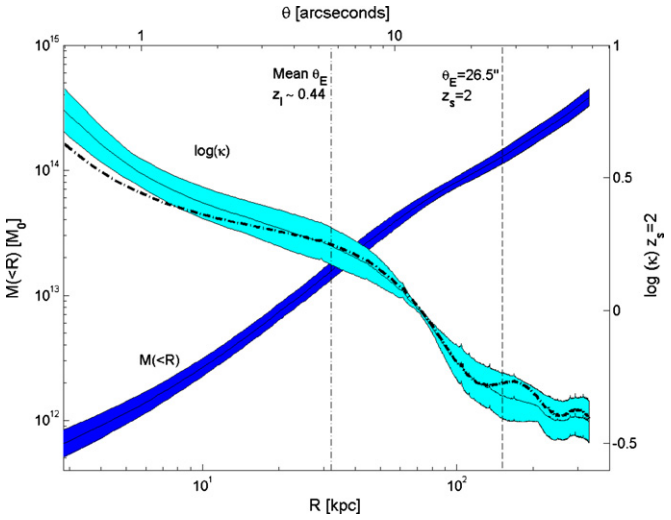

Figure 4. Projected total mass profile. The light blue curve shows the radial surface mass density profile in units of the critical surface density (κ; right-side y-axis), for a source redshift of $z_s = 2$. The dark blue curve shows the overall enclosed mass per radius, $M(< R)$ (left side y-axis). The widths of the blue curves indicate the $\sim 1\sigma$ errors. The thick dash-dotted curve is the (preliminary) best-fit model resulting from a 4×10^4 step Monte Carlo Markov Chain (MCMC) with Metropolis–Hastings algorithm, which allows also the BCG mass to vary. The results are very similar, with only some discrepancy at radii below $\sim 1''$. The details of this MCMC method will be presented elsewhere. The dash-dotted vertical line denotes the mean Einstein radius ($z_s = 2$) distribution from 3000 SDSS clusters at $z \sim 0.44$ (Zitrin et al. 2011b), and the vertical dashed line denotes the Einstein radius of MACS1206 (see Section 4 for this comparison).

(A color version of this figure is available in the online journal.)

Zitrin et al. 2009b, 2010). However, it is not perfectly clear whether MACS1206 is indeed a relaxed cluster; X-ray and optical light contours (see e.g., Ebeling et al. 2009) indeed show an approximately (circularly) symmetric distribution, without a prominent sign of recent merger. However, a high-velocity dispersion (1580 km s^{-1}; Gilmour et al. 2009), along with the excessive X-ray luminosity (2.4×10^{45} erg s^{-1} at [0.1–2.4] keV; $(4.3 \pm 0.1) \times 10^{45}$ erg s^{-1} bolometric, [0.1–100] keV) and temperature (11.6 ± 0.7 keV; see Ebeling et al. 2009; 10.8 ± 0.6 keV; see Postman et al. 2012), may imply a merger along the line of sight (see also Postman et al. 2012). A full assessment of the degree of relaxation of this system will be soon enabled, by the dynamical analysis from several hundreds member velocities we are currently collecting in our spectroscopic program, as well as from the combination of other mass diagnostics.

We note that given its redshift, MACS1206 has a relatively large Einstein radius. Previous studies have shown that other MACS clusters at a redshift of $z \sim 0.5$ distribute around this Einstein radius size ($\theta_E \simeq 28''$), but with a noticeable discrepancy from expectations of the ΛCDM model and related simulations (e.g., Zitrin et al. 2011a; Meneghetti et al. 2011), even after taking into account triaxiality-induced lensing bias.

Recently, we have applied our lens-modeling technique to an unprecedentedly large sample of 10,000 SDSS clusters to deduce a representative distribution of Einstein radii (see Zitrin et al. 2011b), covering the full cluster mass range. As found therein, for the redshift bin corresponding to MACS1206 the distribution for $z_s = 2$ peaks below 10″(with median and mean θ_E of 4.″1 and 5.″6, respectively) and rapidly declines toward larger radii. As may be expected from the different selection criteria, the Einstein radius of the X-ray selected cluster MACS1206 ($\theta_E \simeq 26.''5$ for $z_s = 2$) sits at the (far) tail of the distribution: only ≃1.3% of the optically selected

SDSS clusters examined at this redshift have similar (or larger) Einstein radii, and as much corresponding enclosed mass, as found in MACS1206. The lensing model for MACS1206 presented here, enabled by deep, multi-band *HST* imaging, constitutes an important example of the inner mass distributions of systems lying at the high end of the cluster mass function.

We thank the anonymous reviewer of this manuscript for useful comments. The CLASH Multi-Cycle Treasury Program (GO-12065) is based on observations made with the NASA/ESA *Hubble Space Telescope*. The Space Telescope Science Institute is operated by the Association of Universities for Research in Astronomy, Inc. under NASA contract NAS 5-26555. Part of this work is based on data collected at the Very Large Telescope at the ESO Paranal Observatory, under Programme ID 186.A-0798.

REFERENCES

Arnouts, S., Cristiani, S., Moscardini, L., et al. 1999, MNRAS, 310, 540
Benítez, N. 2000, ApJ, 536, 571
Benítez, N., Ford, H., Bouwens, R., et al. 2004, ApJS, 150, 1
Broadhurst, T., Bentez, N., Coe, D., et al. 2005, ApJ, 621, 53
Broadhurst, T., Umetsu, K., Medezinski, E., Oguri, M., & Rephaeli, Y. 2008, ApJ, 685, L9
Broadhurst, T. J., & Barkana, R. 2008, MNRAS, 390, 1647
Coe, D., Benítez, N., Sánchez, S. F., et al. 2006, AJ, 132, 926
Daddi, E., Dannerbauer, H., Stern, D., et al. 2009, ApJ, 694, 1517
Daddi, E., Dickinson, M., Morrison, G., et al. 2007, ApJ, 670, 156
D'Aloisio, A., & Natarajan, P. 2011, MNRAS, 411, 1628
Ebeling, H., Barrett, E., Donovan, D., et al. 2007, ApJ, 661, L33
Ebeling, H., Edge, A. C., & Henry, J. P. 2001, ApJ, 553, 668
Ebeling, H., Edge, A. C., Mantz, A., et al. 2010, MNRAS, 407, 83
Ebeling, H., Ma, C. J., Kneib, J., et al. 2009, MNRAS, 395, 1213
Fassbender, R., Nastasi, A., Bhringer, H., et al. 2011, A&A, 527, L10
Gilmour, R., Best, P., & Almaini, O. 2009, MNRAS, 392, 1509
Gobat, R., Daddi, E., Onodera, M., et al. 2011, A&A, 526, A133
Halkola, A., Seitz, S., & Pannella, M. 2006, MNRAS, 372, 1425
Hennawi, J. F., Dalal, N., Bode, P., & Ostriker, J. P. 2007, ApJ, 654, 714
Host, O. 2012, MNRAS, 420, L18
Ilbert, O., Arnouts, S., McCracken, H. J., et al. 2006, A&A, 457, 841
Jee, M. J., Dawson, K. S., Hoekstra, H., et al. 2011, ApJ, 737, 59
Jee, M. J., Rosati, P., Ford, H. C., et al. 2009, ApJ, 704, 672
Jullo, E., Natarajan, P., Kneib, J., et al. 2010, Science, 329, 924
Kneib, J. P., Mellier, Y., Fort, B., & Mathez, G. 1993, A&A, 273, 367
Koekemoer, A. M., Faber, S. M., Ferguson, H. C., et al. 2011, ApJS, 197, 36
Koekemoer, A. M., Fruchter, A. S., Hook, R. N., & Hack, W. 2002, in The 2002 *HST* Calibration Workshop: Hubble after the Installation of the ACS and the NICMOS Cooling System, ed. S. Arribas, A. Koekemoer, & B. Whitmore (Baltimore, MD: Space Telescope Science Institute), 337
Limousin, M., Richard, J., Jullo, E., et al. 2007, ApJ, 668, 643
Meneghetti, M., Fedeli, C., Zitrin, A., et al. 2011, A&A, 530, A17
Oguri, M., & Blandford, R. D. 2009, MNRAS, 392, 930
Planck Collaboration, Aghanim, N., Arnaud, M., et al. 2011, A&A, 536, A26
Postman, M., Coe, D., Benitez, N., et al. 2012, ApJS, 199, 25
Richard, J., Kneib, J., Ebeling, H., et al. 2011, MNRAS, 414, L31
Rosati, P., Tozzi, P., Gobat, R., et al. 2009, A&A, 508, 583
Santos, J. S., Fassbender, R., Nastasi, A., et al. 2011, A&A, 531, L15
Williamson, R., Benson, B. A., High, F. W., et al. 2011, ApJ, 738, 139
Zitrin, A., Broadhurst, T., Barkana, R., Rephaeli, Y., & Benítez, N. 2011a, MNRAS, 410, 1939
Zitrin, A., Broadhurst, T., Bartelmann, M., et al. 2011b, arXiv:1105.2295
Zitrin, A., Broadhurst, T., Coe, D., et al. 2011c, MNRAS, 413, 1753
Zitrin, A., Broadhurst, T., Coe, D., et al. 2011d, ApJ, 742, 117
Zitrin, A., Broadhurst, T., Rephaeli, Y., & Sadeh, S. 2009a, ApJ, 707, L102
Zitrin, A., Broadhurst, T., Umetsu, K., et al. 2009b, MNRAS, 396, 1985
Zitrin, A., Broadhurst, T., Umetsu, K., et al. 2010, MNRAS, 408, 1916